POLITECNICO
MILANO 1863

SCUOLA DI INGEGNERIA INDUSTRIALE
E DELL'INFORMAZIONE

Executive Summary of the Thesis

Performance of a VFP Engine: Thermal Evaluation of a Water-cooled Nozzle and Ballistic Analysis

Laurea Magistrale in Aeronautical and Space Engineering - Ingegneria Aeronautica e Spaziale

Author: Davide Fellegara, Luca Pecchini

Advisor: Prof. Christian Paravan

Co-advisor: Eng. Valerio Santolini

Academic year: 2022-2023

1. Introduction

HRE is a thermo-chemical propulsion system that stores fuel in solid form and oxidizer in liquid or gaseous form, offering advantages with respect to Solid Rocket Motors (SRMs) such as direct control of oxidizer mass flow rate and simplicity in design compared to Liquid Rocket Engines (LREs). However, traditional HREs face challenges like low regression rates and high length-to-diameter ratios due to extended propellant mixing requirements, limiting their efficiency [11, 15–17, 19]. The Vortex Flow Pancake (VFP) system, proposed by Gibbon and Haag [7, 8], utilizes tangential oxidizer injection to create a vortex flow field between two solid fuel discs, resulting in a compact engine with improved propellant mixing and thermal protection to chamber walls. This design also reduces the O/F shift phenomenon during combustion, which is a commonly observed drawback in traditional HREs [7, 10, 12, 14]. The Space Propulsion Laboratory (SPLab) at Politecnico di Milano is actively researching the SPLab Vortex Flow Pancake (SVFP), exploring different fuel formulations and studying the effects of operating parameters on fuel regression rates and combustion efficiency [9]. This work specifically focuses on the cooling process of the SVFP engine's nozzle, which features a copper nozzle embedded in an aluminum cooling chamber. While this design allows for multiple and longer firings without significant erosion, it influences engine performance by removing heat from expanding gases. The research aims to understand and characterize this phenomenon through data analysis, thermocouple measurements, and tools such as numerical modeling and CFD analysis.

2. Experimental Setup

2.1. SPLab Vortex Flow Pancake

The VFP hybrid rocket engine at SPLab comprises two flat solid fuel disks encased in AISI-316 stainless steel rings, separated by a tangential injection device with 4 oxidizer channels. The combustion chamber's volume increases during burning due to the regression of the fuel disks. The assembly is secured by top and bottom connection flanges with O-ring gaskets and nuts and bolts. The engine features a convergent-divergent copper nozzle with $\varepsilon = 2$

(A_e/A_t), enveloped by a water-cooling chamber. Water flows through pipes connected to the water pipeline system, causing some energy loss but significantly extending the nozzle's lifespan. The experimental setup includes the engine test bench, coolant and propellant feeding system, and a data acquisition system.

2.2. Test facility

The VFP facility is divided into two main areas. In the first room, the test bench hosts the engine fixed to a vertical sled, along with an array of testing tools. These tools include a pressure sensor on one of the four injection arms, a second pressure sensor axially positioned opposite the nozzle, a load cell in the direction of thrust, and an igniter connected to one of the injection arms. The second room functions as the control center, featuring a data acquisition unit and valves to control the flow of nitrogen, oxygen, and water. The feed system comprises two primary channels: the oxidizer line and the nitrogen purge line, both operating under a feeding pressure of 4 MPa. These lines originate from nitrogen and oxygen pressure tanks in the engine room, extending into the control room. The oxygen line in the control room is equipped with a manual valve for precise mass flow rate control. After passing through these components, the lines return to the engine room, connecting to the four engine injectors. A check valve prevents hazardous back-flow before the lines merge, and after the division, four electrovalves enable precise opening and closing just before the combustion chamber.

3. Materials and Fuel Ingredients

The laboratory's experimental tests involved various fuel compositions, categorized into two main groups: acrylonitrile-butadiene-styrene (ABS) grains and paraffin-based grains, varied in their percentages of SEBS-MA, with a consistent percentage of carbon powder.

3.1. ABS

ABS, a thermoplastic polymer, is chosen for its mechanical and thermal properties, as highlighted by Bisin et al. [5, 6], and its ease of shaping using 3D printing [5–7]. The enthalpy of formation for ABS was characterized by Whitmore et al. [18, 20], providing essential data for computing the characteristic velocity in the NASA CEA code.

3.2. Paraffin

Paraffins belong to hydrocarbons' family, with the general formula C_nH_{2n+2}. This study utilizes SasolWax 0907, a commercial microcrystalline paraffin wax ($C_{50}H_{102}$) produced by Sasol GmbH [1, 2]. With a high melting temperature of $356 - 367$ K and low melt layer viscosity, SasolWax 0907 is chosen for hybrid combustion due to its favorable response to the entrainment effect. The formulation involves mixing paraffin with varying percentages of Styrene-Ethylene-Butylene-Styrene grafted with Maleic Anhydride (SEBS-MA) to achieve a balance between mechanical properties and ballistic performance. Specifically, percentages of $5 - 10 - 20$ wt.% SEBS-MA were employed in this work.

3.3. SEBS-MA

SEBS-MA is a thermoplastic co-polymer commercially produced by Sigma-Aldrich [3]. In this study, it serves as a reinforcing additive to enhance the mechanical properties of the paraffin matrix. The mechanical and thermal properties of SEBS-MA, along with its good compatibility with paraffin, make it a valuable reinforcing ingredient.

3.4. Carbon Powder

Carbon powder (CB) is a graphite micron-sized powder supplied by Sigma-Aldrich [3]. It is added to all paraffin-based compositions at a concentration of 1 wt%. The inclusion of CB offers several advantages, including the enhancement of radiant heat transfer between the flame zone and the surface. Additionally, it prevents the thermal wave from penetrating the bulk of the fuel, thereby preventing degradation of mechanical properties and sloughing of the fuel grain [13].

4. Experimental Procedures

he assembly process initiates with an engine inspection in the workshop. NO and N2 fuel grains are inserted into corresponding metal rings, weighed, and key dimensions are measured. Carbon tubes, inserted into the central

hole of the fuel grains, prevent combustion of the sidewalls. Once completed, the NO side disk and its carbon tube are secured in the upper motor section, ensuring contact with the nozzle. The N2 disk and its tube are added, and the assembly is transported to the firing site. The disks are coupled with an injector ring and securing to a moving sled follow, with connection of water pipes, thermocouple, pressure sensors, and igniter. The igniter, composed of HTPB-AP-based solid propellant on a Kanthal wire. Gas flow is enabled by opening manual valves and tanks. The LabVIEW system is activated for data acquisition, and manual operations are set before initiation by pressing the start button. After reaching the preset burning time, oxygen valves are closed, nitrogen valves are opened to stop combustion, cool the nozzle, and purge the system. Post-test, the operator unplugs the igniter, closes gas tanks, and lifts the engine from the load cell for disassembly. Back in the workshop, fuel disks and carbon tube weights are re-measured, and final masses are recorded. Grains are removed from metal rings, which are cleaned for reuse.

5. Firing-Data processing

During the test, data on pressure, oxygen mass flow rate, thrust, and temperature are saved in *.txt* files. MATLAB® is used for data processing, where files are imported as matrices with time instances in the first column and corresponding values in the second column. The signal undergoes Fourier transform to identify characteristic frequencies. A low-pass filter is used to preserve combustion-induced oscillations while removing instrument noise. However, selecting a low cut-off frequency risks eliminating peaks of interest, and a high cut-off may introduce excessive noise. To address this, a relatively low cut-off is chosen, and any removed peaks are reintroduced by comparing the filtered trace with the original. If the absolute difference surpasses a threshold, the corresponding segment in the original trace is replaced in the filtered trace.

5.1. Pressure

Before applying the pressure trace filter, the raw data graph is plotted. The final instant of combustion, denoted as t_f (just before the nitrogen purge-induced pressure peak), and the initial instant of the burning test, $t_{i,\,70\%}$ (associated with reaching 70% of the maximum pressure in a clean trace), are identified. These instants define the combustion window for calculating average quantities, assuming minimal time delays between thrust, pressure, and mass flow rate traces. The filtered pressure plot, indicating the start and end of firing, is displayed in Figure 1. Notably, at $t = 12$ s, oxygen valves open, and the flow-meter gradually increases until the preset flow rate is reached. Ignition occurs at $t = 35$ s, and at $t = 50$ s, nitrogen valves open, extinguishing the flame and purging the system.

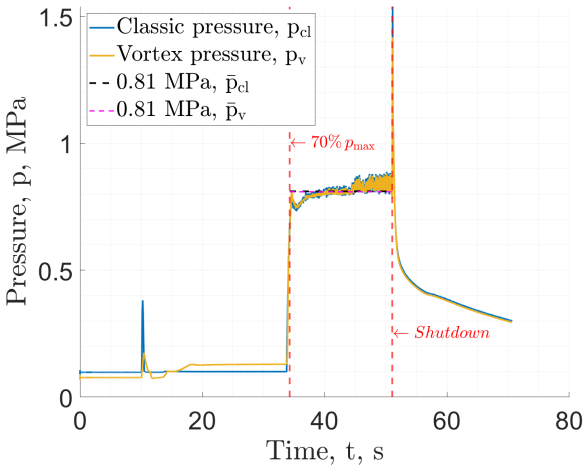

Figure 1: Filtered pressure traces of dual pressure sensor firing, where time 0 is the start of the test

The average pressure (p_{avg}) is computed using the formula:

$$p_{avg} = \frac{1}{\Delta t_b} \int_{\Delta t_b} p(t)\, dt \tag{1}$$

Where the burning time is computed as $\Delta t_b = t_f - t_{i,\,70\%}$. The central pressure sensor (p_v) aims to reveal differences from the vortex-induced pressure (p_{cl}). As depicted in Figure 1, there are no significant distinctions between the two pressure traces.

5.2. Thrust

For the calculation of thrust, it is necessary to subtract the weight of the engine from the value measured by the load cell. The average thrust is then computed as:

$$T_{avg} = \frac{1}{\Delta t_b} \int_{\Delta t_b} T(t)\, dt \tag{2}$$

The burning time (Δt_b) is determined from the pressure trace.

5.3. Oxidizer Mass Flow Rate

The analysis of oxidizer mass flow rate data does not involve filtering. This is due to the low data collection frequency from the device, which is 3 Hz. The burning window is determined from the pressure trace, and the average mass flow rate is calculated as follows:

$$\dot{m}_{ox,avg} = \frac{1}{\Delta t_b} \int_{\Delta t_b} \dot{m}_{ox}(t)\, dt \tag{3}$$

The thrust and the oxidizer mass flow rate plots are shown in Figure 2 and in Figure 3.

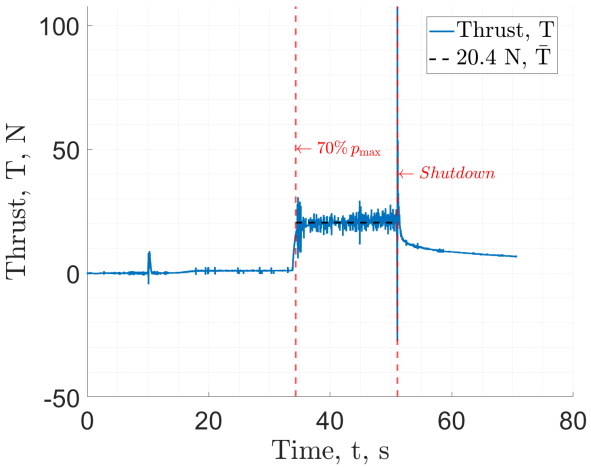

Figure 2: Filtered thrust traces

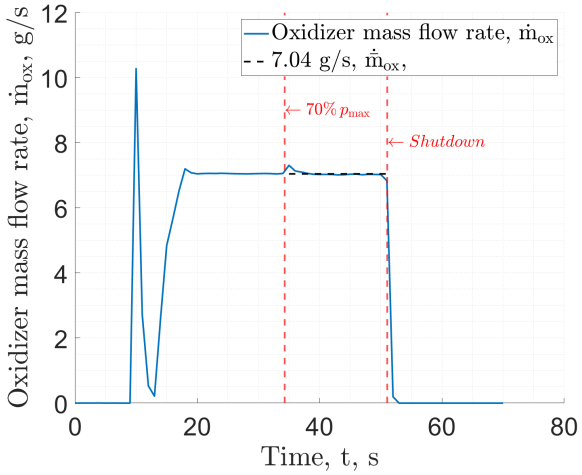

Figure 3: Filtered oxidizer mass flow rate

5.4. Temperatures

The temperature data is obtained from a thermocouple located at the cooling chamber outlet, sampled at 1000 Hz. The transition from the time domain to the frequency domain is achieved through a Fourier transform. Subsequently, a low-pass filter with a cut-off frequency of 0.3 Hz is applied to filter the temperature trace. An example of a water temperature curve is illustrated in Figure 4.

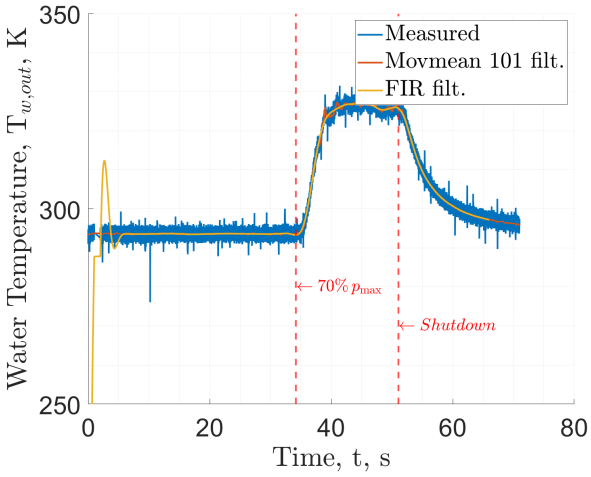

Figure 4: Filtered temperature traces

6. Thermal analysis

The upcoming chapter will focus on developing a thermal model to address the described problem. This will involve implementing the model using MATLAB® code and conducting Computational Fluid Dynamics (CFD) analysis for verification and validation. The complete thermal problem, from the inside to the outside, can be sketched as:

- heat convection between the exaust gases and the nozzle internal surface;
- heat conduction inside the bulk material of the nozzle;
- heat convection between the outer surface of the nozzle and the water inside the chamber;
- heat convection between the water and the aluminium sides of the cooling chamber;
- heat convection between the ambient air and the cooling chamber assembly.

6.1. Thermal problem

The measured water temperature exiting the cooling chamber provides an initial insight into the thermal behavior. As shown in Figure 4, a plateau is reached approximately 5 seconds after a ramping period. The first simplification involves decoupling the top and bottom flanges of the cooling chamber from the nozzle due to the insulating layer and O-ring separating them. The second simplification relates to the water-cooling chamber walls system. Considering the maximum achievable temperature difference between them, the theoretical maximum heat is orders of magnitude lower than the water-nozzle exchange. As a result, the cooling chamber-air heat exchange can be neglected. The third simplification treats the fins as an equivalent surface of the nozzle, considering their short overhang results in approximately 90% efficiency. The last consideration is approximating water and nozzle as two single nodes at uniform temperatures.
To study the thermal problem, the nozzle has been divided into two zones: one subjected to the incoming water flow into the cooling chamber and one that exchanges heat through natural convection with the volume of water occupying the chamber. To estimate the convection coefficients describing these two situations, two empirical correlations for the Nusselt number were used [4]. In particulare the one proposed by Churchill and Bernstein for the cylinder in crossflow and the one proposed by Churchill and Chu [4].
The equation obtained is:

$$\begin{aligned} &\dot{Q}_{wv} = h_{wn} A_n (T_n - T_{wv}) = \\ &= h_{Free}(1-\alpha) A_n (T_n - T_{wv}) + \\ &+ h_{Forced} \alpha A_n (T_n - T_{wv}) \end{aligned} \tag{4}$$

where $\dot{Q}_{wv}$ is the heat power transferred from the nozzle to the water voume, h_{wn} is the generic convective heat transfer coefficient, A_n is the interface surface between nozzle and water, $T_{wv} = (T_{w,in} + T_{w,out})/2$, T_n is the solid wall temperature, h_{Forced} and h_{Free} are the forced and free convective coefficients and α is the unity fraction of the nozzle height on which the water jet impacts (to be determined).

6.2. Numerical formulation

The thermal model previously described was adapted into an algorithm capable of solving the water volume temperature, nozzle temperature, the various heat powers. The code was developed in the MATLAB® environment. To obtain these results, the code needs three parameters to be determined:

- water jet velocity for the forced convection model used to compute the dimensionless numbers expressed in Section 6.1 which must be comprised between 0 and the velocity in the feeding tube;
- fraction of the nozzle (α) exposed to the jet;
- a correction factor for the heat transfer coefficient λ capable of accounting for all the uncertainties in the formulation that is adapted from existing models which might require a correction based on the results of this specific application

6.3. CFD analysis

By using Computational Fluid Dynamics (CFD) correctly, it is possible to simulate complex problems such as the coupled thermal-fluid dynamics of interest. The CFD is a powerful tool that when combined with experimental data can give a correct and detailed view of the system. In this work it is important for the comprehension of the fluid dynamics inside the cooling chamber and therefore for the selection of water jet velocity and α. The thermal analysis can provide a value for λ. The simulation is carried out by setting up a steady-state problem, choice motivated by the fact that the temperature traces collected in the experimental firings reached a plateau roughly five seconds. An example of the CFD analysis can be observed in Figure 5.

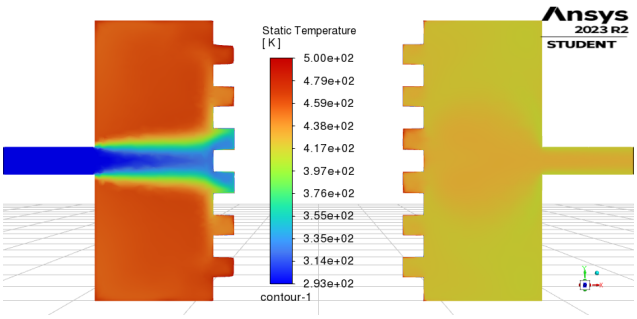

Figure 5: CFD analysis of the cooling chamber's vertical section.

6.4. Algorithm tuning and accuracy

The CFD analysis allowed to finely tune the MATLAB® algorithm based on the formulation taken from the literature in a way that allowed to produce reliable results with the simulations for a wide range of operational conditions so that it can be used on its own to perform predictions and calculations based on the input files only. The CFD allowed to define the previously introduced variables:

- α was set at 0.25;
- the water velocity was set at 3.8 m/s;
- the λ parameter was set at 2.23.

Once the code is calibrated with a sample case of choice representing the best test, it is then verified with other experimental firings, where the maximum relative error in the output temperature was found for the conditions further from the calibration case, but was always below 15%.

7. Results

The final parameters used in the code regarding the water velocity for the cylinder in cross flow, the fraction of chamber assigned to each of the two heat transfer models and the corrective parameter found as a result of the CFD analysis are respectively: 3.8 m/s for the water velocity, 1/4 and 3/4 for the cylinder in cross flow and natural convection models and 2.23 for the corrective parameter for the tuning of the heat transfer coefficients. Thanks to these parameters, it is possible to obtain the temperature of the water and the nozzle, as well as the exchanged thermal power, observable in Figure 6 and in Figure 7.

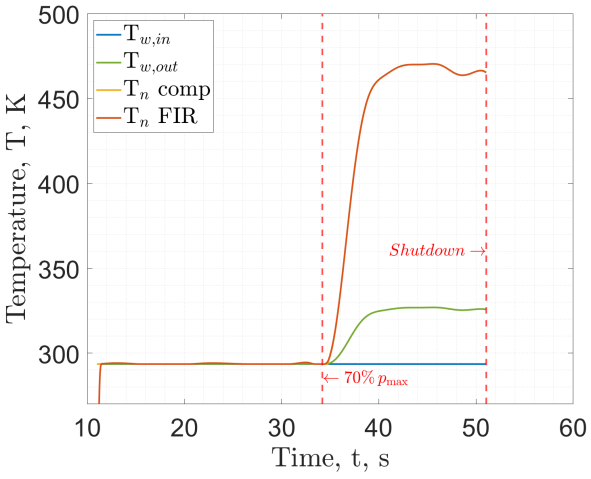

Figure 6: Temperatures.

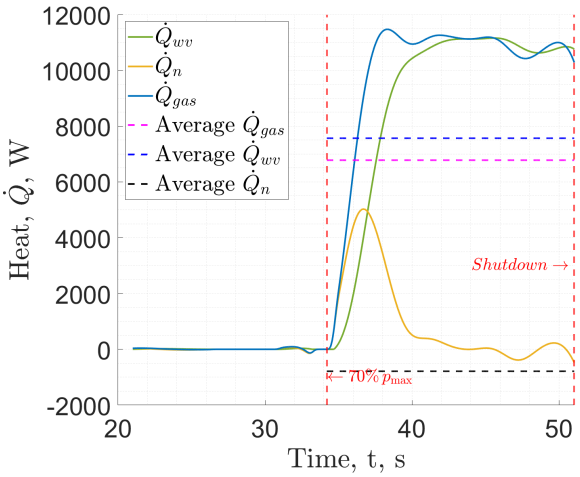

Figure 7: Heat flux magnitude.

8. Conclusions

Results demonstrated that the cooling system is well-designed and maximum predicted nozzle temperatures do not exceed 555 K. Temperature is function of the tested fuel formulation as well of the gas mass flow rate in the nozzle. The results obtained in terms of power subtracted from the gas for the transient case modeled span from 4 to over 13 kW, in accordance with the literature. The produced model is generally accurate, but the hypothesis behind the heat power associated to the nozzle are strong and errors might not be negligible. However, their effect on the final result of the heat loss by the gasses is damped by the biggest contribute coming from water cooling heat transfer, which is from 60 to 90% of the total for the tested conditions. Errors drops with longer firing; for more than 20 seconds, a steady state approximation can be considered.

References

[1] Sasol. https://www.sasol.com/.

[2] Sasol paraffin wax SasolWax 0907. https://www.sasol.com/sasolwax-0907.

[3] Sigma-aldrich. https://www.sigmaaldrich.com/IT/it.

[4] Theodore L Bergman. *Fundamentals of heat and mass transfer*. John Wiley & Sons, 2011.

[5] Riccardo Bisin, Christian Paravan, Sebastiano Alberti, and Luciano Galfetti. A new strategy for the reinforcement of paraffin-based fuels based on cellular structures: The armored grain—mechanical characterization. *Acta Astronautica*, 176:494–509, 2020.

[6] Riccardo Bisin, Alberto Verga, Daniele Bruschi, and Christian Paravan. Strategies for paraffin-based fuels reinforcement: 3d printing and blending with polymers. In *AIAA Propulsion and Energy 2021 Forum*, page 3502, 2021.

[7] Dave M Gibbon and Gary S Haag. Investigation of an alternative geometry hybrid rocket for small spacecraft orbit transfer. *SURREY SATELLITE TECHNOLOGY LTD GUILDFORD (UNITED KINGDOM)*, 2001.

[8] Gary S Haag. *Alternative geometry hybrid rockets for spacecraft orbit transfer*. University of Surrey (United Kingdom), 2001.

[9] Anwer Hashish, Christian Paravan, and Alberto Verga. Liquefying fuel combustion in a lab-scale vortex flow pancake hybrid rocket engine. In *AIAA Propulsion and Energy 2021 Forum*, page 3519, 2021.

[10] MA Karabeyoglu, D Altman, and Brian J Cantwell. Combustion of liquefying hybrid propellants: Part 1, general theory. *Journal of Propulsion and Power*, 18(3):610–620, 2002.

[11] Kenneth K Kuo and Martin J Chiaverini. *Fundamentals of hybrid rocket combustion and propulsion*. American Institute of Aeronautics and Astronautics, 2007.

[12] Christian Paravan, Riccardo Bisin, Francesco Lisi, Luciano Galfetti, and Pietro Massimo. Burning behavior investigation of a vortex flow pancake hybrid rocket engine. In *AIAA Propulsion and Energy 2019 Forum*, page 4418, 2019.

[13] Christian Paravan, Luciano Galfetti, and Filippo Maggi. A critical analysis of paraffin-based fuel formulations for hybrid rocket propulsion. In *53rd AIAA/SAE/ASEE Joint Propulsion Conference*, page 4830, 2017.

[14] Christian Paravan, Jakub Glowacki, Stefania Carlotti, Filippo Maggi, and Luciano Galfetti. Vortex combustion in a lab-scale hybrid rocket motor. In *52nd AIAA/SAE/ASEE Joint Propulsion Conference*, page 4562, 2016.

[15] Christopher St. Clair, Daniel Gramer, Eric Rice, and William Knuth. Advanced cryogenic solid hybrid rocket engine developments-concept and test results. In *34th AIAA/ASME/SAE/ASEE Joint Propulsion Conference and Exhibit*, page 3508, 1998.

[16] George P Sutton and Oscar Biblarz. *Rocket propulsion elements*. John Wiley & Sons, 2016.

[17] Bala Vignesh and Rajiv Kumar. Effect of multi-location swirl injection on the performance of hybrid rocket motor. *Acta Astronautica*, 176:111–123, 2020.

[18] Stephen Whitmore, Zachary Peterson, and Shannon Eilers. Analytical and experimental comparisons of htpb and abs as hybrid rocket fuels. In *47th AIAA/ASME/SAE/ASEE Joint Propulsion Conference & Exhibit*, page 5909, 2011.

[19] Stephen A Whitmore, Sean D Walker, Daniel P Merkley, and Mansour Sobbi. High regression rate hybrid rocket fuel grains with helical port structures. *Journal of Propulsion and Power*, 31(6):1727–1738, 2015.

[20] James R Wilson and Stephen A Whitmore. Pyrolysis of acrylonitrile-butadiene-

styrene (abs) under high heat flux conditions. In *50th AIAA/ASME/SAE/ASEE Joint Propulsion Conference*, page 3752, 2014.